RESEARCH ARTICLE | SEPTEMBER 10 2025

Multifunctional magnonic platform based on the interplay between spin-wave waveguide and nanodots with PMA and DMI

Krzysztof Szulc ; Mateusz Zelent ; Maciej Krawczyk

APL Mater. 13, 091108 (2025)
https://doi.org/10.1063/5.0277362

Multifunctional magnonic platform based on the interplay between spin-wave waveguide and nanodots with PMA and DMI

Cite as: APL Mater. 13, 091108 (2025); doi: 10.1063/5.0277362
Submitted: 23 April 2025 • Accepted: 20 August 2025 •
Published Online: 10 September 2025

Krzysztof Szulc,[1,2,a)] Mateusz Zelent,[2] and Maciej Krawczyk[2]

AFFILIATIONS

[1] Institute of Molecular Physics, Polish Academy of Sciences, M. Smoluchowskiego 17, 60-179 Poznań, Poland
[2] Institute of Spintronics and Quantum Information, Faculty of Physics and Astronomy, Adam Mickiewicz University, Uniwersytetu Poznańskiego 2, 61-614 Poznań, Poland

[a)] **Author to whom correspondence should be addressed:** szulc@ifmpan.poznan.pl

ABSTRACT

Materials with perpendicular magnetic anisotropy (PMA) and antisymmetric exchange interactions are widely explored in spintronics but are of limited use in magnonics due to high damping. We present a hybrid magnonic crystal composed of a chain of circular nanodots with strong PMA and Dzyaloshinskii–Moriya interaction (DMI), positioned above a spin-wave waveguide made of permalloy. Due to the dipolar coupling between the subsystems, a strongly bound hybrid magnetization texture is formed, with two stable magnetization states in the nanodots: a single-domain state and an egg-shaped skyrmion state, allowing reprogramming of the system properties. Numerical results show complex spin-wave spectra with several key features for magnonics: programmable Bragg and non-Bragg bandgaps correlated with magnon–magnon couplings, the flat bands and bound states for the skyrmion state, and exclusively waveguide-dominated modes for the single-domain state. With these properties, the proposed hybrid magnonic crystal has different functionalities that overcome the damping limitations of materials with PMA and DMI and open up potential applications in spin-wave filtering, spin-wave generation, quantum magnonics, and analog magnonics, in particular in the realization of magnonic neural networks.

I. INTRODUCTION

Over the past decade, spin-wave (SW) computing has been extensively researched as a potential candidate to complement and surpass CMOS-based technologies[1,2] for digital[3] or analog signal processing[4,5] and neural network implementation.[6,7] This is because SWs offer high-frequency operation, even at tens of GHz, miniaturization well below 100 nm, and most importantly, ultralow power consumption, as low as 1 aJ per operation. Moreover, they can locally interact with magnetic solitons, i.e., domain walls in 1D[8] and magnetic vortices[9] or skyrmions in 2D[10] and thus can hybridize with, be excited by, and be controlled by soliton dynamics.[8,11]

Magnetic skyrmions are topologically protected 2D magnetization textures, known for their stability and very small size down to 10 nm, especially Néel skyrmions in thin ferromagnetic films, which are stabilized by the interfacial Dzyaloshinskii–Moriya interaction (DMI).[12] Their dynamics can be driven by external forces, such as magnetic field, electric current, structural stress, thermal fluctuations, or laser pulses,[13] which expands their potential applications for information storage and processing, including unconventional computing[14–19] as well as usefulness in magnonics,[10] for instance, to control SW propagation,[20] to scatter SWs,[21,22] to form SW frequency combs,[23] or to excite propagating SWs in thin films.[24] Furthermore, 1D and 2D arrays of skyrmions in thin films form a periodic potential for SWs, and these structures can be considered as reprogrammable magnonic crystals with transmission bands separated by bandgaps.[25–29] However, due to the high damping of SWs in multilayers with DMI,[30,31] and the high frequencies considered so far (tens of GHz)[25] with a few exceptions, these effects remain mainly numerical demonstrations with negligible damping assumed.[27,32]

Hybrid structures are commonly used to obtain systems that combine two, usually mutually exclusive, material properties, such

as ferromagnetism and superconductivity[33,34] or SW propagation and enhanced programmability provided by the artificial spin ice system.[35–37] This is also true for magnonics and skyrmions. The former requires long propagation distances[2] and coherence times[38] and thus low damping, while the latter requires DMI and PMA resulting from spin–orbit interactions and neighboring heavy metals, which is associated with increased damping.

Following these ideas, we propose a hybrid structure consisting of a SW conduit made of a low-damping material (Py) and a chain of nanodots made with strong PMA and DMI material (Ir/Co/Pt), thus also high SW damping. We show in micromagnetic simulations that this structure forms a hybrid magnonic crystal (HMC), which serves as a multifunctional platform for SW applications with properties controlled by the static magnetization configuration—single domain or skyrmion state—of the nanodots. Among the interesting properties arising from the coupling between the two subsystems is a reprogrammable magnonic band structure, where the widths of the Bragg bandgaps are modified by the magnetization texture in the nanodots and flat magnonic bands both below and above the ferromagnetic resonance (FMR) frequency in Py in the case of the skyrmion state. The former property allows SW filtering and the latter enables enhanced nonlinear dynamics,[39] the realization of bound states in the continuum (above FMR of Py) in a magnonic domain[40] or the evanescent coupling between the skyrmion oscillations (below the FMR). Furthermore, we found that a dynamical coupling between clockwise (CW) skyrmion modes and propagating SWs leads to band anticrossing with non-Bragg bandgaps, suitable for exploiting the magnon–magnon coupling and thus useful for excitation of short spin waves, neuromorphic computing[41] and quantum magnonic applications.[42,43] Considering a wide range of interesting properties, the proposed HMC represents a promising multifunctional platform for magnonics, allowing the exploitation of high-damping multilayer materials with PMA and DMI.

II. GEOMETRY OF THE HMC

The system under investigation is presented in Fig. 1. It consists of an infinite permalloy (Py, $Ni_{80}Fe_{20}$) waveguide with width of 300 nm and thickness of 4.5 nm and a chain of Ir/Co/Pt multilayer nanodots with a 300 nm diameter and 1.5 nm thickness. The dots are positioned centrally above the waveguide with a relative separation of 50 nm, resulting in a periodic structure with a lattice constant of 350 nm. The waveguide and the dots are separated by a 3 nm-thick nonmagnetic layer. The study is based on micromagnetic simulations, with SW dynamic simulations performed in linear approximation. The simulation details and the material parameters are provided in Sec. V.

III. RESULTS AND DISCUSSION

A. Static magnetization configuration

In the multilayer nanodot, characterized by strong PMA and DMI, various magnetization states can be stabilized, including an out-of-plane single-domain state, a Néel-type skyrmion, a double-domain structure, and worm-like domains.[44] In this paper, we focus on two of the above-mentioned configurations—a single-domain (SD) state and a skyrmion (Sk) state. While the literature is well-versed in the static and dynamic behavior of these structures in isolation,[45,46] their statics become complex in a compact hybrid system,[47] and the dynamics have not yet been presented.

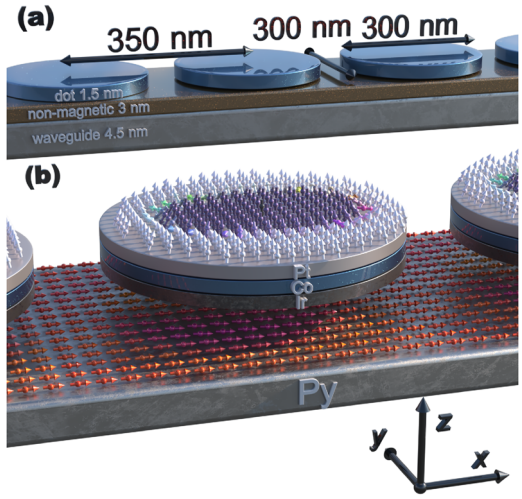

FIG. 1. Visual representation of the system under consideration. (a) A schematic geometry of the Ir/Co/Pt multilayer nanodot, separated from the 4.5 nm-thick Py strip by a 3 nm-thick nonmagnetic layer. (b) An artist's rendering of the simulated magnetization configuration, showing an egg-shaped Néel-type skyrmion in the dot stabilized by magnetostatic coupling to the skyrmion imprint on the in-plane magnetized strip. The arrows and their colors (according to the HSL-cone color scale) indicate the direction of magnetization. Note that the figure is not to scale.

Figure 2 presents the static magnetic configuration of a single unit cell of the HMC with two different magnetization configurations—the waveguide (W) with a chain of nanodots with the out-of-plane SD magnetization state (W/SD) and the waveguide with a chain of nanodots with Sks (W/Sk). The magnetization texture is shown on the xy-planes crossing the center of the dot [(a) and (c)] and the center of the waveguide [(b) and (d)], respectively. In the HMC, the magnetization configuration differs from that of isolated subsystems. This change, induced by the dipolar coupling, is mainly caused by the competition between the strong PMA in the nanodots, which favors magnetization along the z axis, and the shape anisotropy inherent in the waveguide, which induces a preference for magnetization along the x axis.[47]

In the W/SD system, the most pronounced effect of dipolar interaction between the subsystems manifests just beneath the edges of the nanodot, as illustrated in Fig. 2(b). Here, the peak deviation in magnetization reaches $\max|M_{0y}| = 216$ kA/m (i.e., 27% of M_S in Py) along the y axis and $\max|M_{0z}| = 23$ kA/m along the z axis. Notably, within the nanodot itself, the magnetization deviation of ~2% is present close to the nanodot edge.

The static magnetic texture in the W/Sk system undergoes more significant modification. The Sk is not only imprinted in the magnetization of the waveguide but also takes on an egg-like shape instead of being circular.[47] Note that the imprint intensity is stronger in the W/Sk system than in the W/SD system. The average net magnetization along the easy axis in the W/Sk system decreases by 20 kA/m in comparison with only 5 kA/m for the W/SD system. In addition, the maximum deviation reaches $\max|M_{0y}| = 475$ kA/m and $\max|M_{0z}| = 59$ kA/m.

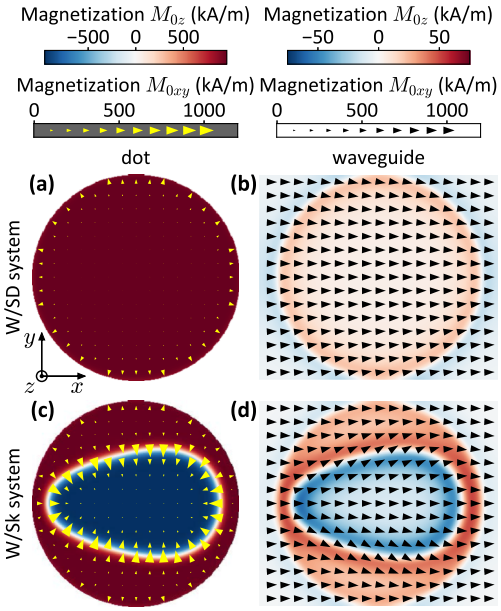

FIG. 2. Configuration of the magnetization in the unit cell of the HMC with nanodots in [(a) and (b)] the SD state and [(c) and (d)] the Sk state. The magnetization is shown in the *xy*-planes crossing [(a) and (c)] the center of the nanodot and [(b) and (d)] the center of the waveguide. The color map shows the M_{0z} component of the magnetization, and the in-plane component M_{0xy} is represented with the arrows.

B. Magnonic band structure

Following analysis of the system's static magnetization configurations, we performed numerical simulations of the SW dynamics (see Sec. V for details). The dispersion relations of W/SD and W/Sk systems are depicted in Figs. 3(a) and 3(b), respectively, where the color map indicates the intensity I of the out-of-plane dynamic magnetization component m_z across the entire system. The intensity of each mode is quantified as follows:

$$I_{\mathrm{mode}}(k, f_n(k)) = \left| \iiint_V m_z(f_n(k)) e^{ikx} \mathrm{d}x\mathrm{d}y\mathrm{d}z \right|^2, \tag{1}$$

where V denotes the volume of magnetic material within a single unit cell and $f_n(k)$ is the frequency of the nth mode at wavevector k, being a complex function. Next, the intensities of all modes are converted into the Lorentzian function and then summed to give the total intensity I,

$$I(k, f) = \sum_n \frac{I_{\mathrm{mode}}(k, f_n(k))}{\mathrm{Im}[f_n(k)]\left(1 + \left(\frac{f - \mathrm{Re}[f_n(k)]}{\mathrm{Im}[f_n(k)]}\right)^2\right)} \tag{2}$$

at wavevector k and frequency f. This method of quantifying intensity makes these results comparable with the Brillouin light scattering measurement results.[48] For comparison, the dispersion relation of an isolated waveguide without a chain of dots is illustrated with the yellow dashed lines and the resonance frequencies of the dot with the blue horizontal lines. The SW modes start at 8.887 GHz and 54 MHz in the first and next systems, respectively. The more detailed comparison between the dispersion relation of the isolated waveguide and the frequencies of the SW modes in the isolated nanodot in the SD and Sk states is presented in Sec. S2 of the supplementary material.

The dispersion relations of both systems contain complex mode dependencies, caused by the interaction between the nanodots and their magnetization imprints in the waveguide. The highest-intensity mode follows the fundamental mode of an isolated waveguide. The antisymmetric waveguide modes are barely visible in the plots due to the nature of the intensity calculation. Above the third waveguide mode, the intensity distribution is unclear and only the fundamental modes are recognizable. The reflected branches and bandgaps are present as a result of the periodicity induced by the arrangement of the nanodots.

However, there are significant differences in the bandgap width of the Bragg gaps among the systems. The zoom-ins of the dispersions of W/SD and W/Sk systems are shown in Figs. 3(c) and 3(d), respectively, with the gray strips marking the positions of the bandgaps. The widths of the first five bandgaps are listed in Fig. 3(e). The W/SD system is characterized by larger low-order gaps, with the size exceeding 400 MHz. The size of higher-order gaps is much smaller, with gap 5 already being similar in size to the linewidth of the modes (which is 77 MHz), making it barely noticeable. In contrast, the W/Sk system is characterized by larger sizes of higher-order bandgaps, i.e., third and higher. Due to the backward wave character of the low-frequency mode at low wavevectors, the edge of the first Brillouin zone lies close to the frequency minimum. As a result, the first and second bands share the same character. In the W/SD system, the stronger interaction between the modes pushes the first band much below the frequency of the isolated waveguide [see Fig. 3(a)]. In the W/Sk system, this interaction is weaker, which causes the first band maximum to be at a higher frequency than the second band minimum, leading to the absence of the bandgap, as shown in Fig. 3(d). These properties clearly demonstrate the reprogrammable nature of the proposed HMC system. By preserving the frequency positions of the bandgaps, we can modify their width and even close or open the first bandgap simply by changing the magnetization state in the dots. This property can be directly used for the realization of the magnonic artificial neural network proposed in Ref. 49, where instead of hard magnets modifying the local magnetic field, the nanodots in the SD or Sk state are used.

An important question is about the mechanisms of the bandgap formation in the W/SD and W/Sk systems. There are two main factors that can be involved in the formation. One is a periodic static configuration. The magnetization imprint in the waveguide coming from the dipolar interaction with the dot enables the Bragg scattering in the system. However, the dynamic coupling between the propagating SWs in the waveguide and the magnetization dynamics confined to the nanodots can also provide such an effect. It is more intuitive when the resonator eigenfrequencies overlap with the continuous bands of the waveguide.[35,50,51] Nevertheless, coupling can also occur when the resonant frequencies of the nanoelements are much higher than the lowest propagation bands of the waveguide.[52,53] In our study, the former situation is realized in the W/Sk system and the latter in the W/SD system.

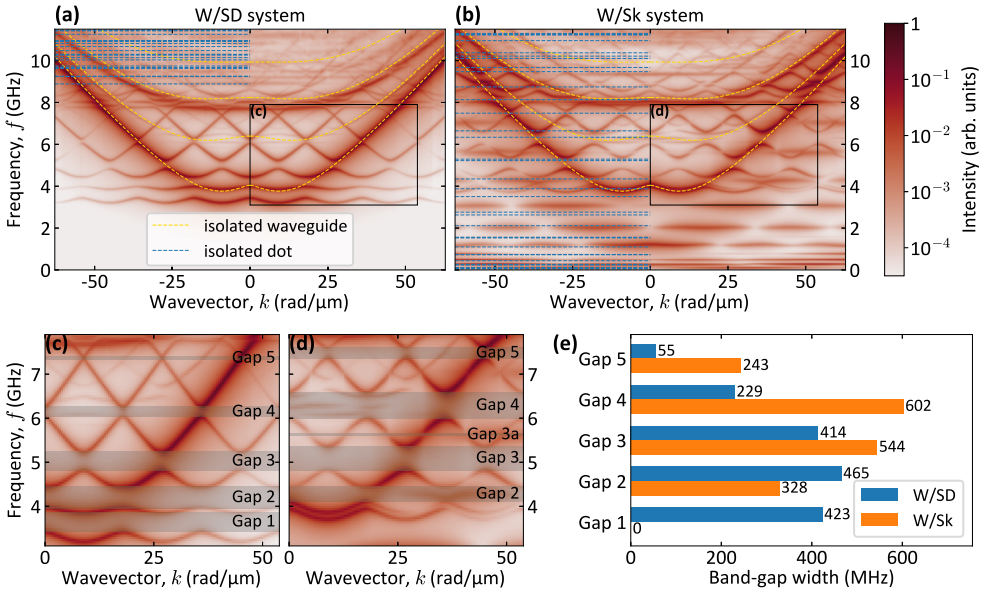

FIG. 3. Dispersion relation of (a) the W/SD system and (b) the W/Sk system. The color maps show the intensity measured for the out-of-plane component of the magnetization m_z. Intensity is scaled logarithmically. The yellow dashed lines indicate the dispersion relation of the waveguide itself without dots and the horizontal blue dashed lines mark the resonance frequencies of a dot in the SD state (a) and Sk state (b). Panels (c) and (d) are zoom-ins of the W/SD and W/Sk systems' dispersion relations as marked by black rectangles in panels (a) and (b), respectively. The gray rectangles mark the Bragg gaps. (e) Bar chart collecting bandgap widths for both W/SD and W/Sk systems.

Another difference between the spectra in both systems is the presence of numerous flat bands in the dispersion of the W/Sk system, which lie below the waveguide modes and begin at frequencies below 1 GHz. These modes are directly connected to the dynamics of the Sk domain wall in the dots, which starts at the level of tens of MHz (see Fig. S2 in the supplementary material). At higher frequencies, some of the skyrmion modes hybridize with the waveguide modes. Interestingly, one of these modes leads to the generation of an additional bandgap with a width of 53 MHz, marked as gap 3a in Fig. 3(d). The modified spectra indicate that the presence of Sks in dots can directly affect the dynamics of SWs propagating in the waveguide. Obviously, such modes are not present in the W/SD system since the lowest resonant mode of the nanodot in an SD state is at the frequency of 8.887 GHz, which is above the third waveguide mode. These results show that the change of a magnetization configuration of the dots can induce additional flat bands in the SW spectrum and also magnon–magnon coupling, effects that are currently under intense investigation and also important from an application point of view.[39,53–60] In Sec. III C, we will explore these properties, focusing on understanding of the physical mechanisms involved.

C. Mode localization

In order to deepen the analysis of the SW dynamics, we calculated the localization of the modes and plotted it on the dispersion relation folded to the first Brillouin zone, as shown in Figs. 4(b) and 4(c). We define the mode localization as a measure of how much of the intensity of a given mode comes from a given subsystem (in this case—a waveguide). It is calculated as

$$L(k, f_n) = \frac{\mathscr{I}_\mathrm{w}}{\mathscr{I}_\mathrm{w} + \mathscr{I}_\mathrm{d}}, \tag{3}$$

where $\mathscr{I}_\mathrm{w}$ and $\mathscr{I}_\mathrm{d}$ are the intensity of the mode in the waveguide and dot, respectively. Intensity is measured as

$$\mathscr{I}_\mathrm{w(d)}(k, f_n) = \iiint_{V_\mathrm{w(d)}} |\mathbf{m}(k, f_n)|^2 \mathrm{d}x\mathrm{d}y\mathrm{d}z, \tag{4}$$

where $V_\mathrm{w(d)}$ is the volume of the waveguide (dot) in a unit cell. The mode fully localized in the dot has a value of $L = 0$ and is indicated in Figs. 4(b) and 4(c) with light blue color, while the mode fully localized in the waveguide has a value of $L = 1$ and is indicated with light brown color. A more extensive description of the mode localization is presented in Sec. S1 of the supplementary material.

Analysis of the SW spectrum will be conducted in three different frequency ranges: range I, marking the frequencies below the SW excitation in the waveguide but available Sk excitation in the dot; range II, where the waveguide can be excited but still only the Sk in the dot; and range III, where the excitation of the whole dot is possible.

The mode localization for the W/SD system is shown in Fig. 4(b). The SW profiles of five selected modes (W/SD-1–W/SD-5) are presented in the first row of Fig. 4(e). In addition, we plot the frequency as a function of localization in Fig. 4(a), with k dependence coded in the following colors: green for $k = 0$ and navy blue for the Brillouin zone boundary. There are no modes existing in range I. This is because the excitations in the isolated subsystems are also not possible here. The W/Sk system is presented in Fig. 4(c). The SW profiles of nine selected modes are presented in two bottom rows of Fig. 4(e). In addition, we plot the frequency as a function of localization in Fig. 4(d).

1. W/SD system—Waveguide modes

In the W/SD system, the lowest mode has a frequency slightly above 3 GHz, and all modes up to 8.9 GHz (range II) are predominantly confined to the waveguide with minimal amplitude in the nanodot. The lowest localization value in this region is $L = 0.89$. This is consistent with the simulations of eigenstates of an isolated nanodot, where the lowest mode was observed at 8.887 GHz

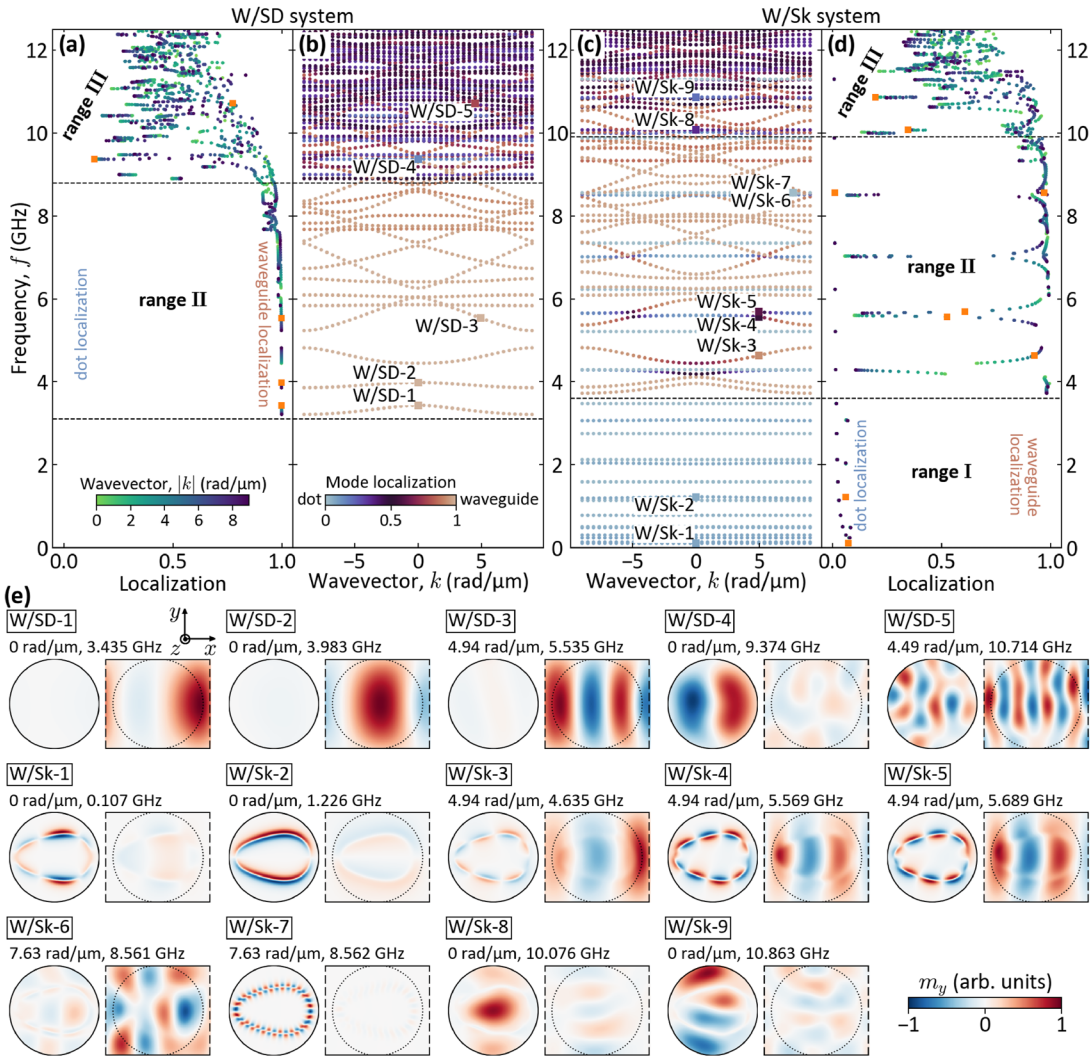

FIG. 4. Dispersion relation in the first Brillouin zone presents the localization of modes in both (b) W/SD and (c) W/Sk systems. Each mode localization value is indicated by the color of the point on the dispersion. The corresponding plots with the localization value are shown in panel (a) for the W/SD system and in panel (d) for the W/Sk system. Here, the color of the point marks the absolute value of the wavevector. The black dashed vertical lines mark the limits of ranges. (e) SW mode profiles for five modes in the W/SD system and nine modes in the W/Sk system. The modes are marked on the dispersion relations with a square point and a label. In each mode profile, the left color map displays the m_y magnetization component in the *xy*-plane at the center of the dot, while the right color map displays m_y in the *xy*-plane at the center of the waveguide. The intensity is normalized so that the maximum value of $|m_y|$ is 1 for each of the mode profiles. All profiles are labeled and their wavevector and frequency are given (Multimedia available online).

(see Sec. S2 in the supplementary material). Consistently, most of the modes in this range resemble typical waveguide modes, e.g., mode W/SD-3. However, selected modes, such as W/SD-1 and W/SD-2, as discussed already in Sec. III B, are coupled over the entire range of the Brillouin zone, resulting in a non-uniform SW amplitude distribution even at $k = 0$. Therefore, the Bragg scattering and bandgap formation in range I in the W/SD system can be attributed to the static magnetization imprint created in the waveguide by the nanodot [see Fig. 2(b)].

2. W/Sk system—Narrow-bandwidth skyrmion modes

In the W/Sk system, range I spans the frequencies from 100 MHz to 3.5 GHz [Figs. 4(c) and 4(d)], which is below the frequency of the lowest waveguide band (see Sec. S2 in the supplementary material). It contains 15 flat bands related to the modes localized in nanodots (the largest localization in this range is $L = 0.08$), which are CW and counterclockwise (CCW) azimuthal modes of the skyrmion domain wall, similar to the skyrmion in an

isolated dot (see Fig. S1 in the supplementary material).[46,61,62] The lowest frequency mode, W/Sk-1, is a third-order CCW mode. The skyrmion breathing mode,[62] W/Sk-2, has a frequency of 1.226 GHz and is only the ninth lowest mode.

The modes in this range have very small bandwidths ranging from 9 kHz to 34 MHz (breathing mode, W/Sk-2). This is because these modes can only interact via dipolar interactions or evanescent SWs, which are the only ones that can exist in the waveguide at such low frequencies. The simulation of the dot chain in the Sk state but without the waveguide (see Table 1 in Sec. S3 of the supplementary material) shows that the bandwidths of most of the bands are significantly smaller in the absence of the waveguide, except for the breathing mode (of comparable bandwidth, 33 MHz) and the fourth CCW mode, which is larger than in the system with the waveguide (further details on this comparison can be found in Sec. S3 of the supplementary material). This suggests the coupling of the Sk modes from range I through the evanescent waves in the waveguide. Such an effect is similar to the enhanced SW transmission observed experimentally in bi-component 1D MC at frequencies below the FMR frequency of one of the constituent materials.[63] However, here, it is theoretically predicted for 1D HMC consisting of a homogeneous film and a chain of dots in the Sk state that the system is easily extendable to a 2D array.

The effects described above could be exploited for the design of frequency-selective magnonic devices at the nanoscale. The evanescent wave coupling between Sk oscillations in nanodots can be exploited for tuning the bandwidth of the collective excitations, extending the possibilities offered by the chain and arrays of Sk nanodots.[28,64] In particular, the distinct localization and narrow bandwidths of these modes offer opportunities to create highly efficient filters or oscillators that operate within a precisely defined frequency range. Furthermore, these weakly dispersive bands can be used to exploit the flat-band physics recently demonstrated in 1D MCs with periodic modulation of a DMI.[39,54] These are expected to create suitable conditions for Bose–Einstein condensation of magnons[65] for predefined and reconfigurable energy landscapes.[66]

3. W/Sk system—Hybridized and bound states

Starting from 3.5 GHz in the W/Sk system, the waveguide modes start to appear and they coexist with Sk modes (range II). Interestingly, the Sk is always slightly excited even if the mode is strongly localized in the waveguide; for instance, the mode W/Sk-3 has a localization $L = 0.925$. Such strong waveguide localization is also found at the edges of the Bragg bandgaps, confirming that their origin is mainly in the imprinted magnetization texture in the waveguide, similar to the W/SD system.

On the one hand, the CW Sk modes hybridize with the waveguide modes, resulting in mixed modes that are present in both the waveguide and the nanodot. In Fig. 4(d), these modes form characteristic horizontally aligned points with localization between 0.05 and about 0.55. As shown before, such hybridization leads to an additional bandgap marked as gap 3a in Fig. 3(d), with the surrounding modes labeled W/Sk-4 and W/Sk-5. This is an example of magnon–magnon coupling, which has recently been studied intensively in many different realizations,[67–69] including skyrmions[10] in the context of the quantum technologies.[70] In our HMC, the hybridization occurs for nonzero k, so it can also provide a protocol for the excitation of propagating modes in the waveguide at a given wavelength by excitation of a specific Sk mode only, locally with single Sk pumped or as a grating coupler with an array of nanodots.[71] Moreover, the resonant coupling offers a possibility for the realization of artificial neural networks,[41,49] where the propagating SWs act as synapses connecting neurons, playing through the nanodot in the Sk or SD state. This will require the activation of neurons by propagating SWs. Such a nonlinear property can be achieved by slightly increasing the SW amplitude so that the static magnetic component decreases, resulting in a change of the resonance frequency (e.g., around the modes W/Sk-4 and W/Sk-5 or around 4 GHz, with a change of just about 10 MHz)[72–74] and, depending on the realization, activating or deactivating of the resonance effect.

On the other hand, CCW Sk modes form a vertical line of points shown in Fig. 4(d) and have strong localization in nanodots with L not exceeding 0.02. Thus, we can conclude that the interaction between the CCW modes and the waveguide modes is negligible. The pair of modes W/Sk-6 and W/Sk-7 around 8.56 GHz differ in frequency by only 1 MHz but their localization values are 0.97 and 0.01, respectively. As expected, the small amplitude in the nanodot for mode W/Sk-6 is not connected with the Sk mode W/Sk-7, further confirming a lack of coupling between them. This suggests the possibility of exploiting these modes, which are strongly localized in the dot but are uncoupled to the waveguide, as bound states in the continuum. Such states are extensively studied in photonics[40] due to enhanced light confinement, sharp Fano resonances, and topological characteristics,[75] but have yet to be explored in magnonics.

4. Range III—Mixed regime

In the frequency range marked as range III, the modes have a mixed character. It starts at 8.9 GHz for the W/SD system and at 10 GHz for the W/Sk system. The higher frequency for the W/Sk system is due to the presence of skyrmion in the dot, which induces specific confinement of the resonant modes in the dot, leading to an increase in their frequency. The localization value in the range varies between 0.13 and 0.96 (after excluding the weakly interacting CCW skyrmion modes), and the range further reduces to 0.14–0.83 above 10.5 GHz in W/SD system and to 0.23–0.82 above 11.5 GHz in the W/Sk system. In this range, there are modes localized predominantly in the nanodot [e.g., mode W/SD-4, W/Sk-8, and W/Sk-9 shown in Fig. 4(e)], which originate from the resonant modes in the isolated nanodot in the SD or Sk state, but they always have energy leakage to the waveguide. On the other hand, the propagating waveguide modes, such as mode W/SD-5, also have significant amplitude in the nanodots. This indicates that in both systems considered, most of the modes in range III are hybrid in nature, combining excitations in the nanodot with modes propagating in the waveguide. This is also the reason for the smeared intensity observed in the band structure in Fig. 3(a), above the dispersion of the fundamental mode. Furthermore, a large number of hybridized modes do not support the formation of bandgaps in range III.

D. Role of damping on band structure in HMC

The results presented above were performed assuming realistic values of damping for Py and multilayer nanodot (see Sec. V), thus we expect to observe the discussed properties under experimental

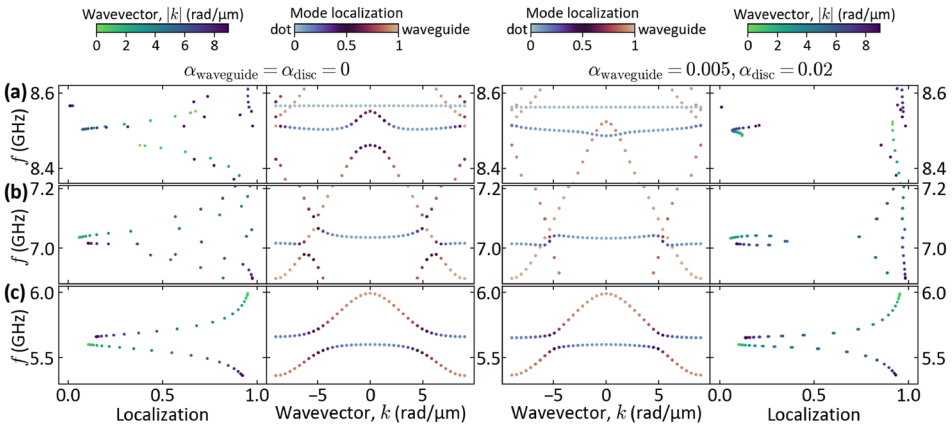

FIG. 5. Dispersion relation in the W/Sk system in the vicinity of (a) sixth CW, (b) fifth CW, and (c) fourth CW skyrmion modes when the damping is neglected (left side) and when it is taken into account (right side). Each mode localization value is indicated by the color of the point on the dispersion (second and third columns). On the localization plots (first and fourth columns), the colors of the points mark the absolute value of the wavevector.

conditions. However, to make the results more general, we perform a study of the magnonic band structure assuming no damping ($\alpha = 0$ for both Py and Ir/Co/Pt multilayer). The detailed comparison of the magnonic band structure of systems with realistic damping values and without damping is shown in Fig. S4 in the supplementary material. We found that damping has a minor impact on the band structure except for the hybridizations between the modes propagating in the waveguide and Sk modes, especially in range II. The zoom-ins to the vicinity of three different Sk modes are shown in Fig. 5 for the case of no damping in both subsystems (left side of the figure) and the case of realistic values of damping (right side of the figure). Around the fourth CW Sk mode [around 5.5 GHz, Fig. 5(c)], the interaction between the modes in both cases leads to the opening of the bandgap. The gap is only slightly larger for the case without the damping (60 MHz) than with the damping (53 MHz). A stronger influence of damping is visible for the sixth CW Sk mode [around 7 GHz, Fig. 5(a)]. Here, the presence of damping leads to a closure of the bandgap. However, despite the gap being closed, the modes are still interacting since the Sk mode is slightly dispersive and its localization reaches the value 0.36. Even more pronounced influence of the damping is shown in Fig. 5(b) for the fifth CW mode (around 8.5 GHz), where the Sk mode opens two bandgaps in the case of no damping, while the presence of damping leads to the closure of these gaps. Here, the coupling is significantly diminished resulting in the separation of modes localized in the dots and the waveguide.

To better understand and quantify the role of damping in the dynamic coupling between the Sk and the waveguide, we calculate the effective damping, defined as ratio of the imaginary part to the real part of the mode frequency $\alpha_{\text{eff}} = \text{Im}(f)/\text{Re}(f)$, for each mode in the HMC. This is done in pairs, comparing α_{eff} for W/SD and W/Sk systems with nominal damping values and comparing nominal damping values and zero damping for the W/Sk system (see Fig. S3 and detailed discussion in Sec. S4 of the supplementary material). A significant change in effective damping leads to changes in the lifetime of the hybridized modes, which is an inverse of the imaginary angular frequency, $T = (\text{Im}(2\pi f))^{-1} = (\alpha_{\text{eff}}\text{Re}(2\pi f))^{-1}$. Interestingly, high damping in the nanodots has a small influence on the collective dynamics in the HMC. The effective damping value follows the value of pristine waveguide, only increasing in the W/Sk system when the waveguide modes are coupled to the Sk modes and in range III when the waveguide and nanodot modes are strongly coupled. For instance, around the fourth CW Sk mode around 5.5 GHz, the effective damping value for the isolated waveguide is about 0.013, while its maximum in the W/Sk system reaches 0.037, reducing the mode lifetime by three times. In summary, the proposed hybrid system reduces the effect of the high damping present in the nanodots and it keeps the lifetime of the modes as low as in the isolated waveguide while having a modulated dispersion relation.

E. Experimental feasibility of the system

The geometry and magnetization configuration are complex, making them challenging to create and study experimentally. The waveguide and dots can be created using the magnetron sputtering method. The final process requires additional steps including the deposition of the resist and lithography (e.g., electron beam, ion beam, or deep ultraviolet) before depositing the magnetic material and removal of the unwanted material with a lift-off technique.[76,77] Bringing the system to the expected magnetic state requires first saturating the system with an external magnetic field, then going to zero field. The magnetic state of the dots can be switched by scanning with a magnetic tip. Numerical analysis has shown that this method can efficiently switch between the single-domain and skyrmion states.[78] An important point is the size of the system. Although the magnonic crystal is infinite in theory, its basic properties should be detectable in arrays as small as ten repetitions.[79] The SW propagation can be measured using different techniques. Brillouin light scattering (BLS) spectroscopy can be used to measure the dispersion relation of the system.[80] SWs can also be excited using a microstrip or coplanar waveguide antenna and detected electrically using second receiving antenna (so called propagating SW spectroscopy),[81] or optically with microfocused BLS,[82] time-resolved magneto-optic Kerr effect (TR-MOKE) microscopy,[83] or scanning transmission x-ray microscopy (STXM).[84]

IV. CONCLUSIONS

We have studied a one-dimensional HMC consisting of an infinitely long Py waveguide and a chain of nanodots with PMA and DMI (Ir/Co/Pt), in which we consider two different magnetic states: a skyrmion and a single-domain state. The static magnetization configuration in the HMC differs from that of its isolated subsystems. This is because the configuration of the dot imprints the magnetization texture upon the waveguide, and at the same time, the skyrmion shape becomes strongly distorted, taking on an egg-like shape. This makes a SW dynamic in an HMC complex while increasing the skyrmion stability and offering multifunctional properties for advancing magnonics.

The dispersion relations of both systems exhibit characteristic features of magnonic crystals such as folded branches and bandgaps that open at the border or center of the Brillouin zone, resulting from the Bragg scattering on the static magnetization imprints in the waveguide. However, there is a substantial difference in the sizes of the bandgaps, demonstrating the programmability of the proposed HMC. In addition, the W/Sk system has a large number of flat low-frequency modes below the resonance frequency of the waveguide. These modes are related to the azimuthal rotating modes, both CW and CCW, localized in the Sk domain wall and are characterized by very narrow bandwidths ranging from single kHz to single MHz. Interestingly, the bandwidths are significantly larger than those of the dots with the Sks forming a chain but without a waveguide, indicating evanescent-SW coupling between the Sks in the W/Sk system. The flat bands may also overlap with the waveguide modes at higher frequencies and, interestingly, depending on their sense of rotation, can hybridize (CW modes) with them, sometimes leading to additional non-Bragg bandgaps in the spectrum, or be uncoupled (CCW modes). Importantly, some of the anticrossing bandgaps in the W/Sk system are preserved even at high damping values in Co/Pt dots. In the same frequency range in the W/SD system, all modes are almost exclusively localized in the waveguide.

The aforementioned properties offer several useful functionalities and potential applications of the proposed HMCs, allowing the magnonic exploitation of the Sk formed in high-damping multilayers. These are (i) exploitation of the Bragg and non-Bragg bandgaps for SW filtering; (ii) coupling between Sk localized modes via evanescent SWs in the Py for controlled SW transmission; (iii) flat bands below the FMR of the Py waveguide with a high density of states for exploitation of nonlinear effects; (iv) flat bands overlapping with the spectra of propagating SWs in Py for exploitation of bound states in the continuum; and (v) magnon–magnon coupling between Sk modes and propagating SWs for quantum and neuromorphic computing. Importantly, the coupling/decoupling depends on the chirality of the Sk mode and all properties can be controlled by reconfiguring the magnetization texture in the nanodots between Sk and SD states, further extending the functionality of HMCs.

V. METHODS

The magnetization dynamics of the system are described by the Landau–Lifshitz–Gilbert equation,

$$\frac{\partial \mathbf{M}}{\partial t} = -|\gamma|\mu_0 \mathbf{M} \times \mathbf{H}_{\text{eff}} + \frac{\alpha}{M_S}\mathbf{M} \times \frac{\partial \mathbf{M}}{\partial t}, \tag{5}$$

where γ is the gyromagnetic ratio, μ_0 is the permeability of vacuum, $\mathbf{H}_{\text{eff}}$ is the effective magnetic field, α is the damping constant, and M_S is the saturation magnetization. The effective magnetic field $\mathbf{H}_{\text{eff}}$ is described as follows:

$$\mathbf{H}_{\text{eff}} = \mathbf{H}_0 + \frac{2A_{\text{ex}}}{\mu_0 M_S^2}\nabla^2 \mathbf{M} + \frac{2K_{\text{PMA}}}{\mu_0 M_S^2} M_z \hat{\mathbf{z}} - \nabla\varphi + \frac{2D}{\mu_0 M_S^2}\left(\frac{\partial M_z}{\partial x}\hat{\mathbf{x}} + \frac{\partial M_z}{\partial y}\hat{\mathbf{y}} - \left(\frac{\partial M_x}{\partial x} + \frac{\partial M_y}{\partial y}\right)\hat{\mathbf{z}}\right), \tag{6}$$

where $\mathbf{H}_0$ is the external magnetic field, A_{ex} is the exchange stiffness constant, K_{PMA} is the perpendicular magnetic anisotropy constant, D is the Dzyaloshinskii–Moriya constant, and φ is the magnetic scalar potential, which can be determined from the formula,

$$\nabla^2\varphi = \nabla \cdot \mathbf{M}, \tag{7}$$

which is derived from Maxwell equations in the magnetostatic approximation.

The system was studied using the finite-element method simulations in COMSOL Multiphysics.[85] The simulations were performed in the 3D model with the implementation of Eqs. (5) and (7). The static magnetization configuration was stabilized in the time-domain simulation with periodic boundary conditions placed at the ends of the unit cell perpendicular to the x axis to introduce the periodicity into the system. For proper calculation of the stray magnetic field, the condition $\varphi = 0$ is applied at a distance of 10 μm from the system. As an initial magnetization configuration, the waveguide is uniformly magnetized along the x axis while the dots are uniformly magnetized along the z axis (for the study of a single-domain state configuration) or have a skyrmion inside (for the study of skyrmion state).[86] The magnetic state relaxation lasts 1 μs. The dispersion relation was calculated using the eigenfrequency solver. For this purpose, the Landau–Lifshitz–Gilbert equation is solved in its linearized form, where the total magnetization vector $\mathbf{M} = \mathbf{M}_0 + \mathbf{m}e^{i\omega t}$ is split to a static component $\mathbf{M}_0 = (M_{0x}, M_{0y}, M_{0z})$ and a dynamic component $\mathbf{m} = (m_x, m_y, m_z)$. The equation takes the form of an eigenvalue equation, where the complex eigenvalues give the frequencies, the dynamic magnetization $\mathbf{m}$ and the dynamic magnetic scalar potential are the eigenvectors, and the wavevector is a sweep parameter. Here, the periodic boundary conditions are replaced by Bloch boundary conditions. The tetrahedral mesh is used with a maximum size of 5 nm in the dot and 7 nm in the waveguide. Outside the magnetic material, the mesh grows with ratio 1.4. On the sides where Bloch boundary condition is applied, we prepared identical triangular meshes.

The material parameters of Py are $M_S = 800$ kA/m, $A_{\text{ex}} = 13$ pJ/m, $D = 0$, $K_{\text{PMA}} = 0$, and $\alpha = 0.005$. The magnetic dot is defined with an effective-medium approach[87–90] as a structure with DMI and PMA, where the three repetitions of the 0.5 nm-thick Ir/Co/Pt multilayer are simulated as a single Co layer with an effective thickness. The effective parameters of the dot are $M_S = 956$ kA/m $A_{\text{ex}} = 10$ pJ/m, $D = -1.6$ mJ/m^2, $K_{\text{PMA}} = 717$ kJ/m^3, and $\alpha = 0.02$. In all calculations, the external magnetic field $\mathbf{H}_0 = 0$.

SUPPLEMENTARY MATERIAL

The supplementary material contains the description of mode localization, the numerical simulations of the dynamics of isolated subsystems, the comparison between the frequencies of skyrmion modes in an isolated dot, a dot chain, and W/Sk system, and study of the impact of damping on the spin-wave dynamics.

ACKNOWLEDGMENTS

K. Szulc and M. Krawczyk acknowledge the financial support from the National Science Centre, Poland, under Grant Nos. UMO-2020/39/I/ST3/02413 and UMO-2021/41/N/ST3/04478. K. Szulc acknowledges the financial support from the Foundation for Polish Science. This work was supported by the EU Research and Innovation Programme Horizon Europe (HORIZON-CL4-2021-DIGITAL-EMERGING-01) under Grant Agreement No. 101070347 (MANNGA).

AUTHOR DECLARATIONS

Conflict of Interest

The authors have no conflicts to disclose.

Author Contributions

Krzysztof Szulc: Conceptualization (equal); Data curation (lead); Formal analysis (lead); Funding acquisition (equal); Investigation (lead); Methodology (lead); Software (lead); Visualization (equal); Writing – original draft (lead); Writing – review & editing (equal). **Mateusz Zelent**: Conceptualization (equal); Investigation (supporting); Validation (lead); Visualization (equal); Writing – original draft (supporting); Writing – review & editing (equal). **Maciej Krawczyk**: Conceptualization (equal); Funding acquisition (equal); Investigation (supporting); Project administration (lead); Supervision (lead); Writing – original draft (supporting); Writing – review & editing (equal).

DATA AVAILABILITY

The data that support the findings of this study are openly available in Zenodo at https://doi.org/10.5281/zenodo.10964849.

REFERENCES

[1] A. V. Chumak, P. Kabos, M. Wu, C. Abert, C. Adelmann, A. O. Adeyeye, J. Akerman, F. G. Aliev, A. Anane, A. Awad, C. H. Back, A. Barman, G. E. W. Bauer, M. Becherer, E. N. Beginin, V. A. S. V. Bittencourt, Y. M. Blanter, P. Bortolotti, I. Boventer, D. A. Bozhko, S. A. Bunyaev, J. J. Carmiggelt, R. R. Cheenikundil, F. Ciubotaru, S. Cotofana, G. Csaba, O. V. Dobrovolskiy, C. Dubs, M. Elyasi, K. G. Fripp, H. Fulara, I. A. Golovchanskiy, C. Gonzalez-Ballestero, P. Graczyk, D. Grundler, P. Gruszecki, G. Gubbiotti, K. Guslienko, A. Haldar, S. Hamdioui, R. Hertel, B. Hillebrands, T. Hioki, A. Houshang, C.-M. Hu, H. Huebl, M. Huth, E. Iacocca, M. B. Jungfleisch, G. N. Kakazei, A. Khitun, R. Khymyn, T. Kikkawa, M. Klaui, O. Klein, J. W. Klos, S. Knauer, S. Koraltan, M. Kostylev, M. Krawczyk, I. N. Krivorotov, V. V. Kruglyak, D. Lachance-Quirion, S. Ladak, R. Lebrun, Y. Li, M. Lindner, R. Macedo, S. Mayr, G. A. Melkov, S. Mieszczak, Y. Nakamura, H. T. Nembach, A. A. Nikitin, S. A. Nikitov, V. Novosad, J. A. Otalora, Y. Otani, A. Papp, B. Pigeau, P. Pirro, W. Porod, F. Porrati, H. Qin, B. Rana, T. Reimann, F. Riente, O. Romero-Isart, A. Ross, A. V. Sadovnikov, A. R. Safin, E. Saitoh, G. Schmidt, H. Schultheiss, K. Schultheiss, A. A. Serga, S. Sharma, J. M. Shaw, D. Suess, O. Surzhenko, K. Szulc, T. Taniguchi, M. Urbanek, K. Usami, A. B. Ustinov, T. van der Sar, S. van Dijken, V. I. Vasyuchka, R. Verba, S. V. Kusminskiy, Q. Wang, M. Weides, M. Weiler, S. Wintz, S. P. Wolski, and X. Zhang, IEEE Trans. Magn. **58**, 0800172 (2022).

[2] Q. Wang, G. Csaba, R. Verba, A. V. Chumak, and P. Pirro, Phys. Rev. Appl. **21**, 040503 (2024).

[3] A. V. Chumak, A. A. Serga, and B. Hillebrands, Nat. Commun. **5**, 4700 (2014).

[4] S. Klingler, P. Pirro, T. Brächer, B. Leven, B. Hillebrands, and A. V. Chumak, Appl. Phys. Lett. **105**, 152410 (2014).

[5] T. Fischer, M. Kewenig, D. A. Bozhko, A. A. Serga, I. I. Syvorotka, F. Ciubotaru, C. Adelmann, B. Hillebrands, and A. V. Chumak, Appl. Phys. Lett. **110**, 152401 (2017).

[6] M.-K. Lee and M. Mochizuki, Phys. Rev. Appl. **18**, 014074 (2022).

[7] O. Lee, T. Wei, K. D. Stenning, J. C. Gartside, D. Prestwood, S. Seki, A. Aqeel, K. Karube, N. Kanazawa, Y. Taguchi, C. Back, Y. Tokura, W. R. Branford, and H. Kurebayashi, Nat. Mater. **23**, 79 (2024).

[8] D. Petti, S. Tacchi, and E. Albisetti, J. Phys. D: Appl. Phys. **55**, 293003 (2022).

[9] S. Wintz, V. Tiberkevich, M. Weigand, J. Raabe, J. Lindner, A. Erbe, A. Slavin, and J. Fassbender, Nat. Nanotechnol. **11**, 948 (2016).

[10] Z. Li, M. Ma, Z. Chen, K. Xie, and F. Ma, J. Appl. Phys. **132**, 210702 (2022).

[11] H. Yu, J. Xiao, and H. Schultheiss, Phys. Rep. **905**, 1 (2021).

[12] A. Fert, V. Cros, and J. Sampaio, Nat. Nanotechnol. **8**, 152 (2013).

[13] M. Lonsky and A. Hoffmann, APL Mater. **8**, 100903 (2020).

[14] H. Vakili, J.-W. Xu, W. Zhou, M. N. Sakib, M. G. Morshed, T. Hartnett, Y. Quessab, K. Litzius, C. T. Ma, S. Ganguly, M. R. Stan, P. V. Balachandran, G. S. D. Beach, S. J. Poon, A. D. Kent, and A. W. Ghosh, J. Appl. Phys. **130**, 070908 (2021).

[15] K. Everschor-Sitte, J. Masell, R. M. Reeve, and M. Kläui, J. Appl. Phys. **124**, 240901 (2018).

[16] C. H. Marrows and K. Zeissler, Appl. Phys. Lett. **119**, 250502 (2021).

[17] D. Prychynenko, M. Sitte, K. Litzius, B. Krüger, G. Bourianoff, M. Kläui, J. Sinova, and K. Everschor-Sitte, Phys. Rev. Appl. **9**, 014034 (2018).

[18] K. M. Song, J.-S. Jeong, B. Pan, X. Zhang, J. Xia, S. Cha, T.-E. Park, K. Kim, S. Finizio, J. Raabe, J. Chang, Y. Zhou, W. Zhao, W. Kang, H. Ju, and S. Woo, Nat. Electron. **3**, 148 (2020).

[19] M. S. N. Tey, X. Chen, A. Soumyanarayanan, and P. Ho, ACS Appl. Electron. Mater. **4**, 5088 (2022).

[20] K.-W. Moon, B. S. Chun, W. Kim, and C. Hwang, Phys. Rev. Appl. **6**, 064027 (2016).

[21] J. Lan and J. Xiao, Phys. Rev. B **103**, 054428 (2021).

[22] K. A. Kotus, M. Moalic, M. Zelent, M. Krawczyk, and P. Gruszecki, APL Mater. **10**, 091101 (2022).

[23] Z. Wang, H. Y. Yuan, Y. Cao, Z.-X. Li, R. A. Duine, and P. Yan, Phys. Rev. Lett. **127**, 037202 (2021).

[24] S. A. Díaz, T. Hirosawa, D. Loss, and C. Psaroudaki, Nano Lett. **20**, 6556 (2020).

[25] F. Ma, Y. Zhou, H. B. Braun, and W. S. Lew, Nano Lett. **15**, 4029 (2015).

[26] J. Kim, J. Yang, Y.-J. Cho, B. Kim, and S.-K. Kim, J. Appl. Phys. **123**, 053903 (2018).

[27] X.-g. Wang, Y.-Z. Nie, Q.-l. Xia, and G.-h. Guo, J. Appl. Phys. **128**, 063901 (2020).

[28] Z. Chen and F. Ma, J. Appl. Phys. **130**, 090901 (2021).

[29] M. Bassotti, R. Silvani, and G. Carlotti, IEEE Magn. Lett. **13**, 6101505 (2022).

[30] A. K. Dhiman, M. Matczak, R. Gieniusz, I. Sveklo, Z. Kurant, U. Guzowska, F. Stobiecki, and A. Maziewski, J. Magn. Magn. Mater. **519**, 167485 (2021).

[31] S. Azzawi, A. T. Hindmarch, and D. Atkinson, J. Phys. D: Appl. Phys. **50**, 473001 (2017).

[32] N. Tang, W. L. N. C. Liyanage, S. A. Montoya, S. Patel, L. J. Quigley, A. J. Grutter, M. R. Fitzsimmons, S. Sinha, J. A. Borchers, E. E. Fullerton, L. DeBeer-Schmitt, and D. A. Gilbert, Adv. Mater. **35**, 2300416 (2023).

[33] I. A. Golovchanskiy, N. N. Abramov, V. S. Stolyarov, P. S. Dzhumaev, O. V. Emelyanova, A. A. Golubov, V. V. Ryazanov, and A. V. Ustinov, Adv. Sci. **6**, 1900435 (2019).

[34] A. P. Petrović, M. Raju, X. Y. Tee, A. Louat, I. Maggio-Aprile, R. M. Menezes, M. J. Wyszyński, N. K. Duong, M. Reznikov, C. Renner, M. V. Milosević, and C. Panagopoulos, Phys. Rev. Lett. **126**, 117205 (2021).

[35]R. Negrello, F. Montoncello, M. T. Kaffash, M. B. Jungfleisch, and G. Gubbiotti, APL Mater. **10**, 091115 (2022).
[36]F. Montoncello, M. T. Kaffash, H. Carfagno, M. F. Doty, G. Gubbiotti, and M. B. Jungfleisch, J. Appl. Phys. **133**, 083901 (2023).
[37]T. Dion, K. D. Stenning, A. Vanstone, H. H. Holder, R. Sultana, G. Alatteili, V. Martinez, M. T. Kaffash, T. Kimura, R. F. Oulton *et al.*, Nat. Commun. **15**, 4077 (2024).
[38]X.-F. Pan, P.-B. Li, X.-L. Hei, X. Zhang, M. Mochizuki, F.-L. Li, and F. Nori, Phys. Rev. Lett. **132**, 193601 (2024).
[39]R. A. Gallardo, D. Cortés-Ortuño, T. Schneider, A. Roldán-Molina, F. Ma, R. E. Troncoso, K. Lenz, H. Fangohr, J. Lindner, and P. Landeros, Phys. Rev. Lett. **122**, 067204 (2019).
[40]C. W. Hsu, B. Zhen, A. D. Stone, J. D. Joannopoulos, and M. Soljačić, Nat. Rev. Mater. **1**, 16048 (2016).
[41]K. G. Fripp, Y. Au, A. V. Shytov, and V. V. Kruglyak, Appl. Phys. Lett. **122**, 172403 (2023).
[42]D. D. Awschalom, C. R. Du, R. He, F. J. Heremans, A. Hoffmann, J. Hou, H. Kurebayashi, Y. Li, L. Liu, V. Novosad, J. Sklenar, S. E. Sullivan, D. Sun, H. Tang, V. Tyberkevych, C. Trevillian, A. W. Tsen, L. R. Weiss, W. Zhang, X. Zhang, L. Zhao, and C. W. Zollitsch, IEEE Trans. Quantum Eng. **2**, 5500836 (2021).
[43]Y. Li, W. Zhang, V. Tyberkevych, W.-K. Kwok, A. Hoffmann, and V. Novosad, J. Appl. Phys. **128**, 130902 (2020).
[44]I. V. Vetrova, M. Zelent, J. Šoltýs, V. A. Gubanov, A. V. Sadovnikov, T. Ščepka, J. Dérer, R. Stoklas, V. Cambel, and M. Mruczkiewicz, Appl. Phys. Lett. **118**, 212409 (2021).
[45]A. Riveros, F. Tejo, J. Escrig, K. Y. Guslienko, and O. Chubykalo-Fesenko, Phys. Rev. Appl. **16**, 014068 (2021).
[46]M. Mruczkiewicz, P. Gruszecki, M. Krawczyk, and K. Y. Guslienko, Phys. Rev. B **97**, 064418 (2018).
[47]M. Zelent, M. Moalic, M. Mruczkiewicz, X. Li, Y. Zhou, and M. Krawczyk, Sci. Rep. **13**, 13572 (2023).
[48]J. F. Cochran and J. R. Dutcher, J. Magn. Magn. Mater. **73**, 299 (1988).
[49]Á. Papp, W. Porod, and G. Csaba, Nat. Commun. **12**, 6422 (2021).
[50]M. Mruczkiewicz, P. Graczyk, P. Lupo, A. Adeyeye, G. Gubbiotti, and M. Krawczyk, Phys. Rev. B **96**, 104411 (2017).
[51]P. Graczyk, M. Krawczyk, S. Dhuey, W.-G. Yang, H. Schmidt, and G. Gubbiotti, Phys. Rev. B **98**, 174420 (2018).
[52]H. Qin, R. B. Holländer, L. Flajsman, F. Hermann, R. Dreyer, G. Woltersdorf, and S. van Dijken, Nat. Commun. **12**, 2293 (2021).
[53]Y. Wang, W. Yan, N. Kuznetsov, L. Flajšman, H. Qin, and S. van Dijken, Phys. Rev. Appl. **22**, 014038 (2024).
[54]S. Tacchi, J. Flores-Farías, D. Petti, F. Brevis, A. Cattoni, G. Scaramuzzi, D. Girardi, D. Cortés-Ortuno, R. A. Gallardo, E. Albisetti, G. Carlotti, and P. Landeros, Nano Lett. **23**, 6776 (2023).
[55]G. Centała and J. W. Kłos, Sci. Rep. **13**, 12676 (2023).
[56]J. Wang, H. Wang, J. Chen, W. Legrand, P. Chen, L. Sheng, J. Xia, G. Lan, Y. Zhang, R. Yuan, J. Dong, X. Han, J.-P. Ansermet, and H. Yu, Phys. Rev. Appl. **21**, 044024 (2024).
[57]J. Chen, C. Liu, T. Liu, Y. Xiao, K. Xia, G. E. W. Bauer, M. Wu, and H. Yu, Phys. Rev. Lett. **120**, 217202 (2018).
[58]M. Moalic, M. Zelent, K. Szulc, and M. Krawczyk, Sci. Rep. **14**, 11501 (2024).
[59]P. K. Pal, S. Majumder, Y. Otani, and A. Barman, Adv. Quantum Technol. **6**, 2300003 (2023).
[60]B. Hu, Z.-K. Xie, J. Lu, and W. He, Appl. Phys. Lett. **124**, 232402 (2024).
[61]C. Jin, S. Li, H. Zhang, R. Wang, J. Wang, R. Lian, P. Gong, and X. Shi, New J. Phys. **24**, 043005 (2022).
[62]J.-V. Kim, F. Garcia-Sanchez, J. Sampaio, C. Moreau-Luchaire, V. Cros, and A. Fert, Phys. Rev. B **90**, 064410 (2014).
[63]H. Qin, G.-J. Both, S. J. Hämäläinen, L. Yao, and S. van Dijken, Nat. Commun. **9**, 5445 (2018).
[64]M. Mruczkiewicz, P. Gruszecki, M. Zelent, and M. Krawczyk, Phys. Rev. B **93**, 174429 (2016).
[65]S. O. Demokritov, V. E. Demidov, O. Dzyapko, G. A. Melkov, A. A. Serga, B. Hillebrands, and A. N. Slavin, Nature **443**, 430 (2006).
[66]M. R. Schweizer, A. J. E. Kreil, G. von Freymann, B. Hillebrands, and A. A. Serga, J. Appl. Phys. **132**, 183908 (2022).
[67]K. Adhikari, S. Choudhury, S. Barman, Y. Otani, and A. Barman, Nanotechnology **32**, 395706 (2021).
[68]J. C. Gartside, A. Vanstone, T. Dion, K. D. Stenning, D. M. Arroo, H. Kurebayashi, and W. R. Branford, Nat. Commun. **12**, 2488 (2021).
[69]Y. Wang, Y. Zhang, C. Li, J. Wei, B. He, H. Xu, J. Xia, X. Luo, J. Li, J. Dong, W. He, Z. Yan, W. Yang, F. Ma, G. Chai, P. Yan, C. Wan, X. Han, and G. Yu, Nat. Commun. **15**, 2077 (2024).
[70]Z. Jiang, J. Lim, Y. Li, W. Pfaff, T.-H. Lo, J. Qian, A. Schleife, J.-M. Zuo, V. Novosad, and A. Hoffmann, Appl. Phys. Lett. **123**, 130501 (2023).
[71]H. Yu, G. Duerr, R. Huber, M. Bahr, T. Schwarze, F. Brandl, and D. Grundler, Nat. Commun. **4**, 2702 (2013).
[72]P. Krivosik and C. E. Patton, Phys. Rev. B **82**, 184428 (2010).
[73]H. Merbouche, B. Divinskiy, K. O. Nikolaev, C. Kaspar, W. H. P. Pernice, D. Gouéré, R. Lebrun, V. Cros, J. Ben Youssef, P. Bortolotti, A. Anane, S. O. Demokritov, and V. E. Demidov, Sci. Rep. **12**, 7246 (2022).
[74]Q. Wang, R. Verba, B. Heinz, M. Schneider, O. Wojewoda, K. Davídková, K. Levchenko, C. Dubs, N. J. Mauser, M. Urbánek, P. Pirro, and A. V. Chumak, Sci. Adv. **9**, eadg4609 (2023).
[75]M. Kang, T. Liu, C. T. Chan, and M. Xiao, Nat. Rev. Phys. **5**, 659 (2023).
[76]J. F. Smyth, S. Schultz, D. R. Fredkin, D. P. Kern, S. A. Rishton, H. Schmid, M. Cali, and T. R. Koehler, J. Appl. Phys. **69**, 5262 (1991).
[77]N. Singh, S. Goolaup, and A. O. Adeyeye, Nanotechnology **15**, 1539 (2004).
[78]M. Zelent, I. V. Vetrova, J. Šoltýs, X. Li, Y. Zhou, V. A. Gubanov, A. V. Sadovnikov, T. Ščepka, J. Dérer, R. Stoklas, V. Cambel, and M. Mruczkiewicz, Nanomaterials **11**, 2627 (2021).
[79]P. Frey, A. A. Nikitin, D. A. Bozhko, S. A. Bunyaev, G. N. Kakazei, A. B. Ustinov, B. A. Kalinikos, F. Ciubotaru, A. V. Chumak, Q. Wang, V. S. Tiberkevich, B. Hillebrands, and A. A. Serga, Commun. Phys. **3**, 17 (2020).
[80]G. Gubbiotti, S. Tacchi, M. Madami, G. Carlotti, A. O. Adeyeye, and M. Kostylev, J. Phys. D: Appl. Phys. **43**, 264003 (2010).
[81]M. Bailleul, D. Olligs, C. Fermon, and S. O. Demokritov, Europhys. Lett. **56**, 741 (2001).
[82]T. Sebastian, K. Schultheiss, B. Obry, B. Hillebrands, and H. Schultheiss, Front. Phys. **3**, 35 (2015).
[83]I. Neudecker, K. Perzlmaier, F. Hoffmann, G. Woltersdorf, M. Buess, D. Weiss, and C. H. Back, Phys. Rev. B **73**, 134426 (2006).
[84]J. Gräfe, M. W. Markus Weigand, B. V. Waeyenberge, A. Gangwar, F. Groß, F. Lisiecki, J. Rychly, H. Stoll, N. Träger, J. Förster, F. Stobiecki, J. Dubowik, J. Klos, M. Krawczyk, C. H. Back, E. J. Goering, and G. Schütz, SPIE **11090**, 1109025 (2019).
[85]K. Szulc, S. Tacchi, A. Hierro-Rodríguez, J. Díaz, P. Gruszecki, P. Graczyk, C. Quirós, D. Markó, J. I. Martín, M. Vélez, D. S. Schmool, G. Carlotti, M. Krawczyk, and L. M. Álvarez Prado, ACS Nano **16**, 14168 (2022).
[86]K. Y. Guslienko and Z. V. Gareeva, J. Magn. Magn. Mater. **442**, 176 (2017).
[87]M. Zelent, J. Tóbik, M. Krawczyk, K. Y. Guslienko, and M. Mruczkiewicz, Phys. Status Solidi RRL **11**, 1700259 (2017).
[88]I. Lemesh and G. S. D. Beach, Phys. Rev. B **98**, 104402 (2018).
[89]S. Woo, K. Litzius, B. Krüger, M.-Y. Im, L. Caretta, K. Richter, M. Mann, A. Krone, R. M. Reeve, M. Weigand, P. Agrawal, I. Lemesh, M.-A. Mawass, P. Fischer, M. Kläui, and G. S. D. Beach, Nat. Mater. **15**, 501 (2016).
[90]A. Suna, J. Appl. Phys. **59**, 313 (1986).